

Fuzzy Dark Matter and the Impact of Core–Halo Diversity on Its Particle Mass Constraints

DAFA WARDANA ¹, KOHEI HAYASHI ^{2, 1, 3}, MASASHI CHIBA ¹ AND ELISA G. M. FERREIRA ⁴

¹*Astronomical Institute, Tohoku University, Sendai, Miyagi, 980-0845, Japan*

²*National Institute of Technology, Sendai College, Sendai, Miyagi, 989-3128, Japan*

³*ICRR, The University of Tokyo, Kashiwa, Chiba, 277-8582, Japan*

⁴*Kavli IPMU (WPI), UTIAS, The University of Tokyo, Kashiwa, Chiba, 277-8583, Japan*

ABSTRACT

We investigate how diversity in the core–halo mass relation affects constraints on the fuzzy dark matter particle mass m_ψ inferred from the internal kinematics of dwarf galaxies. Using stellar line-of-sight velocities and projected positions for eight Milky Way dwarf spheroidal galaxies, we model their dark matter halos as solitonic cores embedded within outer NFW envelopes. We apply both second- and fourth-order Jeans analyses to derive the posterior distribution of m_ψ . Our results show that there are two ranges of m_ψ consistent with the observed kinematics: $-20.3 < \log_{10}(m_\psi/\text{eV}) < -19.2$, and a narrower small-mass window $-22.1 < \log_{10}(m_\psi/\text{eV}) < -21.5$, both within the 68% credible intervals. The latter becomes prominent only if core–halo diversity is taken into account. These constraints pose a challenge to fuzzy dark matter, as the small- m_ψ window is in conflict with Milky Way satellite abundances, and our upper bound largely excludes the parameter space permitted by Lyman- α forest constraints.

Keywords: Dark matter (353) — Dwarf spheroidal galaxy (420) — Stellar kinematics (1608)

1. INTRODUCTION

The small-scale challenges faced by the standard Λ -cold dark matter (CDM) paradigm (J. S. Bullock & M. Boylan-Kolchin 2017), together with the persistent lack of direct detection of CDM particles⁵, have motivated renewed interest in alternative dark matter models. Among these, fuzzy dark matter (FDM)—an ultra-light bosonic dark matter candidate with a characteristic particle mass of $m_\psi \sim 10^{-22}$ eV—has emerged as a compelling scenario (W. Hu et al. 2000). Owing to its minimal parameter space, in which the particle mass uniquely determines the phenomenology (H.-Y. Schive et al. 2014a), constraining m_ψ is a central task (see e.g., L. Hui et al. (2017); E. G. M. Ferreira (2021); L. Hui (2021); A. Eberhardt & E. G. M. Ferreira (2025) for comprehensive reviews).

A defining feature of FDM is its kiloparsec-scale de Broglie wavelength, which has profound consequences for structure formation (H.-Y. Schive et al. 2014a; P. Mocz et al. 2017; S. May & V. Springel 2021; M. Nori

& M. Baldi 2021). On cosmological scales, wave interference suppresses the growth of density perturbations below a characteristic mass threshold, reducing the abundance of low-mass halos and potentially alleviating the missing satellites problem (H.-Y. Schive et al. 2014a). On galactic scales, the same wave nature gives rise to an effective quantum pressure that counteracts gravitational collapse, preventing the formation of steep central cusps. Instead, FDM halos develop soliton cores—stable, ground-state solutions of the Schrödinger–Poisson equations—characterized by flat central density profiles (V. H. Robles & T. Matos 2012; H.-Y. Schive et al. 2014a), which provides a natural resolution to the core–cusp problem.

Dwarf spheroidal galaxies (dSphs) and ultra-faint dwarf galaxies (UFDs) in the Milky Way halo are particularly powerful laboratories because they exhibit the highest known mass-to-light ratios of any galaxy type (A. W. McConnachie 2012; G. Battaglia & C. Nipoti 2022). These extreme mass-to-light ratios indicate strong dark matter domination, which minimizes baryonic complications and enables direct probes of the underlying dark matter potential. Moreover, FDM predicts that soliton cores are larger and dynamically more

Email: dafaward@astr.tohoku.ac.jp

⁵ However, see T. Totani (2025) for a recent report on a possible dark matter detection.

significant in less massive halos, further enhancing the sensitivity of dwarf galaxies to the FDM particle mass.

Probing the internal mass distribution of individual dwarfs can be performed through stellar kinematics analysis (S. L. Zoutendijk et al. 2021; K. Hayashi et al. 2021; I. S. Goldstein et al. 2022). This approach relies critically on the relation between the soliton core mass M_c and the host halo mass M_{200} , first reported by H.-Y. Schive et al. (2014a,b) in the form of $M_c \propto M_{200}^{1/3}$. Subsequent kinematic analyses have widely adopted this relation as a one-to-one mapping when inferring the FDM particle mass.

However, the universality of this core–halo mass relation (CHR) has been investigated in more detail. Independent simulations have reported differing slopes (P. Mocz et al. 2017; M. Mina et al. 2022; M. Nori & M. Baldi 2021) or failed to recover a clear scaling altogether (B. Schwabe et al. 2016). These discrepancies have been attributed to limitations in simulation volume and resolution (S. May & V. Springel 2021), as well as to the dynamical state of halos, with unrelaxed systems exhibiting systematic deviations from the original relation (M. Nori & M. Baldi 2021). More recent work has demonstrated that FDM halos populate a broad region in the M_c – M_{200} plane rather than a narrow relation, reflecting genuine physical diversity driven by variations in merger histories, relaxation states, and cosmological environments (H. Y. J. Chan et al. 2022).

The recognition of this intrinsic diversity has important implications for particle-mass constraints. Constraints derived under the assumption of a unique CHR may be artificially restrictive, potentially excluding values of m_ψ that remain compatible with stellar kinematic data when alternative combinations of M_c and M_{200} are permitted. This motivates a reassessment of FDM particle mass estimates that explicitly incorporates the diversity of the CHR predicted by simulations.

In this work, we investigate how allowing for such diversity affects constraints on the FDM particle mass inferred from the internal kinematics of Milky Way dSphs. By marginalizing over a broad family of CHR consistent with cosmological simulations, we aim to provide a physically motivated estimation of the allowed range of m_ψ .

This paper is organized as follows. In Section 2, we describe the FDM halo model adopted in this work, including the soliton and Navarro-Frenk-White (NFW) density profile and its scaling relations. Section 3 presents the dwarf galaxy sample, the kinematic data, and the analysis methodology. In Section 4, we present the resulting constraints on the FDM particle mass. Section 5 discusses these results and compares them with constraints

from other independent probes. Finally, Section 6 summarizes our conclusions.

2. THE MODEL

Under the assumptions of dynamical equilibrium and spherical symmetry, the motion of stars in a gravitational potential $\Phi(r)$ is fully described by the phase-space distribution function $f(\mathbf{r}, \mathbf{v})$. In practice, however, the distribution function is not directly observable. Instead, the Jeans equations provide a means to relate the underlying gravitational potential to observable stellar kinematics through moments of the distribution function.

In spherical coordinates (r, θ, ϕ) , the velocity moments are defined as

$$\overline{\nu v_r^i v_\theta^j v_\phi^k} = \int d^3v v_r^i v_\theta^j v_\phi^k f, \quad (1)$$

where $\nu(r)$ is the three-dimensional stellar density distribution and r denotes the radial distance from the system center. The second-order Jeans equation then takes the form (J. Binney & S. Tremaine 2008)

$$\frac{d}{dr} (\nu \sigma_r^2) + 2 \frac{\beta}{r} \nu \sigma_r^2 + \nu \frac{d\Phi}{dr} = 0, \quad (2)$$

with $\sigma_r(r)$ denoting the radial velocity dispersion. Under spherical symmetry, $\sigma_\theta = \sigma_\phi$, which allows the stellar velocity anisotropy to be defined as $\beta(r) \equiv 1 - \sigma_\theta^2(r)/\sigma_r^2(r)$.

Solving Equation (2) for $\sigma_r(r)$ under the assumption of a constant velocity anisotropy, $\beta(r) = \beta$ for simplicity, and projecting the solution along the line-of-sight (LOS) yields the observable LOS velocity dispersion profile

$$\sigma_{\text{los}}^2(R) = \frac{2}{I(R)} \int_R^\infty dr \left(1 - \beta \frac{R^2}{r^2}\right) \frac{\nu \sigma_r^2 r}{\sqrt{r^2 - R^2}}, \quad (3)$$

in which R is the projected radius, $I(R)$ is the projected stellar density profile derived from $\nu(r)$, and $\sigma_{\text{los}}(R)$ is the LOS velocity dispersion. Throughout this work, we adopt a Plummer profile for the stellar density (H. C. Plummer 1911), given by $I(R) = (\pi r_h^2)^{-1} [1 + R^2/r_h^2]^{-2}$, where r_h is the projected half-light radius.

Due to projection along the LOS, LOS velocity distributions are generally non-Gaussian (J. Binney & M. Merrifield 1998). Therefore, describing LOS velocity distributions solely by their velocity dispersion amounts to approximating a non-Gaussian distribution by its closest Gaussian, which can introduce biases in dynamical inferences (see J. I. Read et al. (2021) for a demonstration). Higher-order velocity moments provide a means to quantify deviations from Gaussianity, with increasing moment order encoding progressively ‘fine-grained’

details of the LOS velocity distribution shape. Because dwarf spheroidal galaxies are primarily dispersion-supported systems, we only incorporate symmetric deviations from Gaussianity and characterize them using the fourth-order velocity moments.

The fourth-order Jeans equation for a spherically symmetric system is given by

$$\frac{d}{dr} \nu \overline{v_r^4} + \frac{2\beta}{r} \nu \overline{v_r^4} + 3\nu \sigma_r^2 \frac{d\Phi}{dr} = 0, \quad (4)$$

where $\overline{v_r^4}$ stands for the fourth-order velocity moment. Projecting the solution of Equation (4) along the LOS under the assumption of constant β yields (E. L. Łokas 2002; G. Battaglia et al. 2013)

$$\begin{aligned} \overline{v_{\text{los}}^4}(R) &= \frac{2}{I(R)} \int_R^\infty dr \\ &\times \left[1 - 2\beta \frac{R^2}{r^2} + \frac{1}{2}\beta(1+\beta) \frac{R^4}{r^4} \right] \frac{\nu \overline{v_r^4} r}{\sqrt{r^2 - R^2}}. \end{aligned} \quad (5)$$

For convenience, the fourth-order LOS velocity moments are expressed in terms of the LOS kurtosis,

$$\kappa_{\text{los}}(R) = \frac{\overline{v_{\text{los}}^4}(R)}{\sigma_{\text{los}}^4(R)} \quad (6)$$

(M. R. Merrifield & S. M. Kent 1990; E. L. Łokas 2002).

A Gaussian velocity distribution corresponds to $\kappa_{\text{los}} = 3$, while $\kappa_{\text{los}} < 3$ and $\kappa_{\text{los}} > 3$ indicate distributions with thinner and heavier tails than a Gaussian, respectively.

Fourth-order velocity moments have been shown to be effective in mitigating the mass–anisotropy degeneracy, primarily because of their sensitivity to the velocity anisotropy parameter (G. Battaglia et al. 2013; A. Genina et al. 2020; D. Wardana et al. 2025; A. Bañares-Hernández et al. 2025). This degeneracy persists in kinematic analyses within the FDM framework (A. X. González-Morales et al. 2017; I. S. Goldstein et al. 2022), even though the model assumes an intrinsically cored density profile. In the FDM context, the mass–anisotropy degeneracy manifests as a degeneracy between the velocity anisotropy and the core radius, which directly impacts the inferred FDM particle mass since r_c is tightly linked to m_ψ through the scaling relations discussed in Section 2.2. Incorporating fourth-order velocity moments is therefore expected to help exclude regions of parameter space in which acceptable fits to the velocity dispersion are achieved only at the cost of, from the perspective of LOS kurtosis, implausible velocity anisotropy. In this work, we incorporate fourth-order velocity moments built upon the dynamical model described in D. Wardana et al. (2025), employing uniform and Laplacian kernels to introduce flexibility in the LOS

velocity distribution shape. The use of such kernels was originally introduced by J. L. Sanders & N. W. Evans (2020).

2.1. Dark Matter Density Profiles

FDM halos naturally develop a central soliton core as the ground-state solution of the Schrödinger–Poisson equation. Based on numerical simulations, H.-Y. Schive et al. (2014a) provided an empirical form for the density profile of FDM halos,

$$\rho_{\text{sol}}(r) = \rho_c \left[1 + 0.091 \left(\frac{r}{r_c} \right)^2 \right]^{-8}, \quad (7)$$

where the core radius r_c is defined as the radius at which the density drops to one-half of its central value ρ_c . The corresponding core density is given by

$$\rho_c \approx 1.9 \times 10^{12} \left(\frac{m_\psi}{10^{-23} \text{ eV}} \right)^{-2} \left(\frac{r_c}{\text{pc}} \right)^{-4} [\text{M}_\odot \text{ pc}^{-3}]. \quad (8)$$

Equation (7) provides an accurate description of the density profile out to radii of a few r_c (H.-Y. Schive et al. 2014b; H. Y. J. Chan et al. 2022). At larger radii, the density departs from the soliton solution and transitions to an NFW-like profile, which can be approximated as

$$\rho(r) = \rho_s \left(\frac{r}{r_s} \right)^{-1} \left(1 + \frac{r}{r_s} \right)^{-2}, \quad (9)$$

where ρ_s and r_s denote the characteristic NFW density and scale radius, respectively.

Accordingly, the halo density profile is modeled as a two-component structure. Defining r_t as the transition radius, the inner region ($r < r_t$) follows the soliton profile, while the outer region ($r \geq r_t$) follows the NFW profile (J. F. Navarro et al. 1997). In this work, the two components are related by imposing continuity of the density at the transition radius,

$$\begin{aligned} \rho_c \epsilon &\equiv \rho_c \left[1 + 0.091 \left(\frac{r_t}{r_c} \right)^2 \right]^{-8} \\ &= \rho_s \left(\frac{r_t}{r_s} \right)^{-1} \left(1 + \frac{r_t}{r_s} \right)^{-2}. \end{aligned} \quad (10)$$

With ϵ and r_s specified, the scale density ρ_s is uniquely determined, as well as r_t is given by $r_t = 0.091^{-1/2} (\epsilon^{-1/8} - 1)^{1/2} r_c$.

2.2. Scaling relations in FDM cosmology

Numerical simulations of FDM consistently predict a well-defined relation between the soliton core mass

M_c and its characteristic radius r_c (H.-Y. Schive et al. 2014b; H. Y. J. Chan et al. 2022),

$$a^{1/2}M_c \approx \frac{5.5 \times 10^{12}}{(m_\psi/10^{-23} \text{ eV})^2 (a^{1/2}r_c/\text{pc})} [M_\odot], \quad (11)$$

where $a = 1/(1+z)$ is the cosmological scale factor, and z is the redshift. This relation implies that more massive soliton cores are correspondingly more compact, reflecting the balance between gravity and quantum pressure.

In addition to the core mass–core radius scaling, simulations have identified a correlation between the soliton core mass and the host halo mass, commonly expressed as $M_c \propto M_{200}^\eta$ (H.-Y. Schive et al. 2014b; P. Mocz et al. 2017; M. Nori & M. Baldi 2021). While the existence of such a correlation appears robust, its slope and normalization exhibit substantial scatter across simulations. To capture this intrinsic diversity, we adopt the generalized CHR proposed by H. Y. J. Chan et al. (2022),

$$a^{1/2}M_c = \xi \left(\frac{m_\psi}{8 \times 10^{-23} \text{ eV}} \right)^{-3/2} + \left(\sqrt{\frac{\zeta(z)}{\zeta(0)} \frac{M_{200}}{\mu}} \right)^\eta \left(\frac{m_\psi}{8 \times 10^{-23} \text{ eV}} \right)^{\frac{3(\eta-1)}{2}} M_\odot, \quad (12)$$

where M_{200} is the halo mass enclosed within the radius at which the mean density equals 200 times the critical density of the Universe. The parameters (ξ, μ, η) encode the normalization, characteristic mass scale, and slope of the relation, respectively. Best-fit values derived from large-volume cosmological simulations are $\xi = 8.00_{-6.00}^{+0.52} \times 10^6 M_\odot$, $\log_{10}(\mu/M_\odot) = -5.73_{-8.38}^{+2.38}$, and $\eta = 0.515_{-0.189}^{+0.130}$, with the quoted uncertainties reflecting the intrinsic scatter among simulated halos.

To incorporate this diversity into our analysis, we draw N_{CHR} independent realizations of the parameter set (ξ, μ, η) , generating a corresponding ensemble of CHR that uniformly populate the $\log_{10}(M_c)$ – $\log_{10}(M_{200})$ plane within the scatter reported by H. Y. J. Chan et al. (2022). In this work, we adopt $N_{\text{CHR}} = 500$ to ensure a smooth and minimally discrete sampling of the relation space. Although a fully probabilistic treatment of the core–halo mass distribution would be more realistic, the limited number of simulated halos and their incomplete coverage motivate this approach, which nevertheless allows us to quantify the impact of CHR diversity on constraints of m_ψ .

3. DATA AND ANALYSIS

Table 1 presents the observational properties of the eight dSphs analyzed in this study: Carina, Draco, Fornax, Leo I, Leo II, Sculptor, Sextans, and Ursa Minor.

The table includes columns for the galaxy name, central photometric coordinates (Right Ascension and Declination), the number of stars in the kinematic sample, heliocentric distance, projected half-light radius, systemic velocities, and associated references. For the purposes of this analysis, the projected half-light radius and systemic velocities are treated as fixed input parameters.

The stellar kinematic samples employed in this study are drawn from the literature. For the Carina, Draco, Ursa Minor, Leo I, and Leo II dSphs, we adopt the spectroscopic datasets presented by M. Fabrizio et al. (2016); M. G. Walker et al. (2015); M. E. Spencer et al. (2018); M. Mateo et al. (2008), and M. E. Spencer et al. (2017), respectively. The kinematic data for Sextans, Sculptor, and Fornax are taken from M. G. Walker et al. (2009a,b). For each system, we retain only stars classified as members in the original analyses, and we do not attempt to redefine or re-evaluate the membership selection. The membership criteria, therefore, follow those adopted in the respective observational studies.

We assume that stars behave as tracer particles within a gravitational potential dominated by dark matter, as dSphs are dark-matter dominated even in their inner regions (A. W. McConnachie 2012; G. Battaglia & C. Nipoti 2022). We further assume that the contribution of binary stars to the observed kinematics is minimal in dSphs⁶ (Q. E. Minor 2013; M. E. Spencer et al. 2017; J. M. Arroyo-Polonio et al. 2023; W. Wang et al. 2023).

Given the available kinematic samples for eight Milky Way dSphs, we fit the model parameters using the following likelihood function

$$\log(\mathcal{L}_{\text{total}}) = \log(\mathcal{L}_{v_{\text{los}}}) + \log(\mathcal{L}_{c_{200}}), \quad (13)$$

where the first term quantifies the likelihood of the observed stellar projected positions R and LOS velocities v_{los} ,

$$\mathcal{L}_{v_{\text{los}}} = \prod_{i=1}^N \frac{1}{(\delta v_{\text{los},i}^2 + \sigma_{\text{los},i}^2)^{1/2}} f_s(w_i), \quad (14)$$

with

$$w_i^2 = \frac{(v_{\text{los},i} - v_{\text{sys}})^2}{\delta v_{\text{los},i}^2 + \sigma_{\text{los},i}^2}. \quad (15)$$

The choice of the kernel function $f_s(w)$ is determined by the predicted LOS kurtosis κ_{los} . Specifically, a uniform

⁶ Despite being more dark matter dominated than dSphs, the low velocity dispersion in UFDs makes them more susceptible to contamination from unidentified binary stars (A. W. McConnachie & P. Côté 2010; E. N. Kirby et al. 2013, 2017; C. Pianta et al. 2022; J. María Arroyo-Polonio et al. 2026). Therefore, given the additional complexities in analyzing UFDs, this study is restricted to dSphs.

Table 1. Observational Properties of the Classical MW’s dSphs

Galaxy Name	RA [hh:mm:ss]	Dec [dd:mm:ss]	N_{star}	M_* [$10^6 M_\odot$]	D_\odot [kpc]	r_h [pc]	v_{sys} [km s^{-1}]	Ref.
Carina	06:41:36.7	−50:57:58	1086	0.38	106 ± 6	308 ± 23	+220.7	(1), (4), (11)
Draco	17:20:12.4	+57:54:55	468	0.29	76 ± 6	214 ± 2	−290.0	(1), (2), (9)
Fornax	02:39:59.3	−34:26:57	2523	20	147 ± 12	838 ± 3	+55.2	(1), (4), (12)
Leo I	10:08:28.1	+12:18:23	177	5.5	254 ± 15	270 ± 2	+282.9	(1), (6), (13)
Leo II	11:13:28.8	+22:09:06	328	0.74	233 ± 14	171 ± 2	+78.7	(1), (7), (14)
Sculptor	01:00:09.4	−33:42:33	1360	2.3	86 ± 6	280 ± 1	+111.4	(1), (8), (12)
Sextans	10:13:03.0	−01:36:53	445	0.44	86 ± 4	413 ± 3	+224.3	(1), (5), (12)
Ursa Minor	15:08:08.5	+67:13:21	318	0.29	76 ± 3	407 ± 2	−246.9	(1), (3), (10)

References: (1) R. R. Muñoz et al. (2018); (2) A. Z. Bonanos et al. (2004); (3) R. Carrera et al. (2002);

(4) G. Pietrzyński et al. (2009); (5) M. G. Lee et al. (2009); (6) M. Bellazzini et al. (2004); (7) M. Bellazzini et al. (2005);

(8) G. Pietrzyński et al. (2008); (9) M. G. Walker et al. (2015); (10) M. E. Spencer et al. (2018); (11) M. Fabrizio et al. (2016);

(12) M. G. Walker et al. (2009a); (13) M. Mateo et al. (2008); (14) A. Koch et al. (2007).

kernel is adopted when $\kappa_{\text{los}} < 3$, while a Laplacian kernel is used when $\kappa_{\text{los}} > 3$.

The second term in Equation (13) incorporates a prior on the halo concentration–mass relation. This relation was originally reported in the CDM simulations (F. Prada et al. 2012; T. Ishiyama et al. 2021). In FDM cosmologies, the suppression of small-scale power delays halo formation, leading to deviations from the CDM concentration–mass relation, as shown analytically by A. Laroche et al. (2022); H. Kawai et al. (2024) and demonstrated in simulations by P.-Y. Liao et al. (2025). However, in the present analysis, the difference between the FDM and CDM concentration–mass relations has a negligible impact. We therefore adopt, for simplicity, the empirical CDM concentration–mass relation for subhalos proposed by Á. Moliné et al. (2017),

$$C_{200}(M_{200}, x_{\text{sub}}) = c_0 \times \left\{ 1 + \sum_{i=1}^3 \left[a_i \log_{10} \left(\frac{M_{200}}{10^8 h^{-1} M_\odot} \right) \right]^i \right\} \times [1 + b \log_{10}(x_{\text{sub}})], \quad (16)$$

where the constants are $c_0 = 19.9$, $b = -0.54$, and $a_{i=1,2,3} = (-0.195, 0.089, 0.089)$. The dimensionless subhalo position parameter is defined as $x_{\text{sub}} \equiv r_{\text{sub}}/r_{200,\text{host}}$, where r_{sub} denotes the subhalo’s distance from the host halo center and $r_{200,\text{host}}$ is the virial radius of the host halo. We require the outer NFW halo to satisfy this concentration–mass relation, yielding the likelihood

$$-2 \log(\mathcal{L}_{c_{200}}) = \frac{[\log_{10}(c_{200}) - \log_{10}(C_{200})]^2}{\sigma_{c_{200}}^2}, \quad (17)$$

where C_{200} is the median subhalo concentration given by Equation (16), $\sigma_{c_{200}} = 0.13$, and c_{200} is computed from the free parameters (r_s, M_{200}).

The full model contains five free parameters over which we marginalize: β , m_ψ , M_{200} , ϵ , and r_s . We adopt log-flat priors for all parameters, with ranges

1. $-1 < -\log_{10}(1 - \beta) < 1$,
2. $-24 \leq \log_{10}(m_\psi/\text{eV}) \leq -18$,
3. $6 \leq \log_{10}(M_{200}/M_\odot) \leq 12$,
4. $-7 \leq \log_{10}(\epsilon) < 0$, which corresponds to $0 < r_t/r_c \leq 8.45$,
5. $-1 \leq \log_{10}(r_s/r_h) \leq 3$.

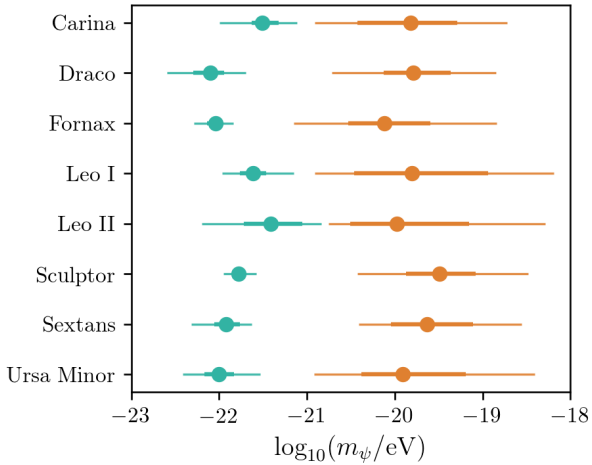
The posterior distributions of the free parameters are sampled using the Markov Chain Monte Carlo (MCMC) method within the Metropolis–Hastings framework (N. Metropolis et al. 1953; W. K. Hastings 1970). We employ a custom-built code developed specifically for this analysis. Convergence of the MCMC chains is assessed through visual inspection. For each galaxy, the MCMC setup consists of 500 walkers, each generating 5000 samples. The first 2000 samples are discarded as burn-in to remove dependence on the initial conditions.

4. RESULTS

Figure 1 presents the inferred values of m_ψ for each analyzed dSph with thick and thin error bars indicating the 68% and 95% credible intervals, respectively. All galaxies exhibit a bimodal posterior distribution in m_ψ , with systems that have larger kinematic samples tending to show more clearly separated high-probability regions. In the figure, the solution peaking at smaller m_ψ

Table 2. Constraints on Model Parameters from Milky Way dSph Satellites

Galaxy	$-\log_{10}(1-\beta)$	$\log_{10}(m_\psi/\text{eV})$	$\log_{10}(M_{200}/M_\odot)$	r_t/r_c	$\log_{10}(r_s/[\text{kpc}])$	$\log_{10}(r_c/[\text{kpc}])$
small-m_ψ						
Carina	$0.10^{+0.16}_{-0.24}$	$-21.51^{+0.19}_{-0.12}$	$8.57^{+0.33}_{-0.26}$	$2.87^{+0.70}_{-0.82}$	$-0.11^{+0.17}_{-0.17}$	$-0.41^{+0.09}_{-0.14}$
Draco	$-0.05^{+0.24}_{-0.11}$	$-22.10^{+0.15}_{-0.20}$	$9.44^{+0.36}_{-0.25}$	$2.75^{+0.79}_{-1.10}$	$0.04^{+0.14}_{-0.15}$	$-0.14^{+0.13}_{-0.09}$
Fornax	$-0.01^{+0.13}_{-0.08}$	$-22.04^{+0.07}_{-0.10}$	$9.13^{+0.24}_{-0.18}$	$2.81^{+0.69}_{-0.71}$	$0.18^{+0.20}_{-0.18}$	$-0.06^{+0.08}_{-0.06}$
Leo I	$-0.05^{+0.22}_{-0.23}$	$-21.61^{+0.15}_{-0.15}$	$8.81^{+0.34}_{-0.25}$	$2.87^{+0.70}_{-0.82}$	$0.02^{+0.15}_{-0.15}$	$-0.42^{+0.11}_{-0.12}$
Leo II	$0.11^{+0.28}_{-0.34}$	$-21.41^{+0.35}_{-0.31}$	$8.70^{+0.44}_{-0.34}$	$2.65^{+0.85}_{-0.68}$	$-0.02^{+0.17}_{-0.18}$	$-0.58^{+0.20}_{-0.28}$
Sculptor	$0.00^{+0.13}_{-0.14}$	$-21.78^{+0.07}_{-0.08}$	$9.00^{+0.37}_{-0.22}$	$2.94^{+0.67}_{-0.76}$	$-0.02^{+0.15}_{-0.16}$	$-0.30^{+0.06}_{-0.06}$
Sextans	$0.06^{+0.19}_{-0.19}$	$-21.92^{+0.16}_{-0.13}$	$9.02^{+0.41}_{-0.29}$	$2.91^{+0.74}_{-0.78}$	$-0.03^{+0.15}_{-0.15}$	$-0.07^{+0.10}_{-0.12}$
Ursa Minor	$0.15^{+0.24}_{-0.24}$	$-22.00^{+0.17}_{-0.17}$	$9.16^{+0.38}_{-0.26}$	$2.80^{+0.92}_{-0.82}$	$-0.00^{+0.14}_{-0.15}$	$-0.10^{+0.12}_{-0.13}$
large-m_ψ						
Carina	$-0.14^{+0.12}_{-0.15}$	$-19.82^{+0.53}_{-0.61}$	$8.67^{+0.46}_{-0.42}$	$3.08^{+0.70}_{-1.12}$	$0.01^{+0.15}_{-0.16}$	$-2.06^{+0.78}_{-0.45}$
Draco	$-0.15^{+0.11}_{-0.10}$	$-19.79^{+0.43}_{-0.33}$	$8.82^{+0.44}_{-0.54}$	$3.20^{+0.61}_{-0.70}$	$0.25^{+0.12}_{-0.11}$	$-2.20^{+0.44}_{-0.43}$
Fornax	$-0.14^{+0.08}_{-0.07}$	$-20.12^{+0.52}_{-0.41}$	$8.78^{+0.36}_{-0.43}$	$3.08^{+0.65}_{-0.76}$	$0.28^{+0.12}_{-0.10}$	$-1.88^{+0.48}_{-0.44}$
Leo I	$-0.27^{+0.18}_{-0.15}$	$-19.80^{+0.86}_{-0.66}$	$8.68^{+0.45}_{-0.47}$	$3.05^{+0.75}_{-0.99}$	$-0.02^{+0.17}_{-0.18}$	$-2.15^{+0.72}_{-0.73}$
Leo II	$-0.16^{+0.42}_{-0.23}$	$-19.98^{+0.81}_{-0.53}$	$8.52^{+0.60}_{-0.54}$	$3.09^{+0.77}_{-0.92}$	$-0.10^{+0.22}_{-0.22}$	$-2.03^{+0.64}_{-0.69}$
Sculptor	$-0.14^{+0.08}_{-0.07}$	$-19.49^{+0.41}_{-0.38}$	$8.68^{+0.41}_{-0.41}$	$3.28^{+0.51}_{-0.77}$	$0.17^{+0.11}_{-0.12}$	$-2.37^{+0.47}_{-0.40}$
Sextans	$-0.12^{+0.12}_{-0.10}$	$-19.63^{+0.52}_{-0.41}$	$8.64^{+0.32}_{-0.34}$	$3.10^{+0.58}_{-0.61}$	$0.05^{+0.13}_{-0.13}$	$-2.16^{+0.46}_{-0.48}$
Ursa Minor	$0.05^{+0.20}_{-0.14}$	$-19.91^{+0.71}_{-0.46}$	$8.76^{+0.51}_{-0.44}$	$3.16^{+0.66}_{-0.70}$	$0.00^{+0.15}_{-0.16}$	$-2.09^{+0.51}_{-0.56}$

**Figure 1.** The estimated m_ψ from this work for each galaxy. There are two high-probability regions, which correspond to two different DM core radii. Thick (thin) error bars indicate 68% (95%) credible interval.

values (corresponding to relatively large DM cores) is shown in green, while the solution favoring larger m_ψ values (corresponding to smaller DM cores) is shown in orange⁷. Thick and thin error bars represent the 68% and 95% credible intervals, respectively. We summa-

⁷ The share of posterior probability mass contained in the two regimes ranges from small- m_ψ /large- m_ψ = 0.49/0.51 to 0.86/0.14.

rize the constraints on the model parameters obtained in this analysis in Table 2, where the quoted uncertainties correspond to the 68% credible intervals. The full posterior distributions of all parameters and recovery of the observed kinematics are presented in Appendix A.

This bimodality in m_ψ arises because the steep density decline of the soliton profile, $\rho(r) \propto r^{-16}$ beyond r_c , is not favored by the stellar kinematic data. Such a rapidly declining density profile produces significantly lower LOS velocity dispersions than both the NFW profile and the inner core of the soliton profile (see Appendix A for a demonstration). Consequently, the model tends to avoid configurations in which many kinematic samples lie within the transition region between r_c and r_t . This behavior gives rise to two viable configurations: either (i) most kinematic samples lie in the NFW-like region ($r > r_t$), or (ii) most kinematic samples reside within the soliton core.

The first scenario corresponds to the high-probability region at relatively large particle masses, $m_\psi \sim 10^{-20}$ eV. In this case, the inferred transition radius lies between 10 and 30 pc, which does not exceed the radius enclosing 1% of the kinematic samples in each galaxy. In contrast, the second configuration requires a substantially larger core, giving rise to the posterior peak at $m_\psi \sim 10^{-22}$ eV. This requirement is reflected in the correlation between the dark matter core radius r_c and the median projected stellar radius, shown in Figure 2. This correlation underscores the importance of identify-

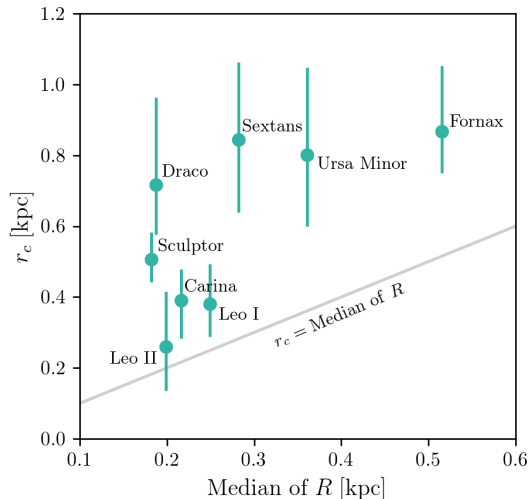


Figure 2. Core radius r_c of the small- m_ψ solutions as a function of the median projected galactocentric distance of the kinematic samples. Error bars denote the 68% credible intervals. The solid gray line represents $r_c = \text{median}(R)$ to guide the readers. For the small- m_ψ solution, the dark matter (DM) core radius must be sufficiently large to encompass most of the kinematic tracers within the core region, which gives rise to the observed correlation.

ing kinematic samples that extend well beyond the currently available radial coverage, such as those that will be provided by the Subaru Prime Focus Spectrograph (PFS) survey (M. Takada et al. 2014; N. Tamura et al. 2016). If the stellar LOS velocity dispersion and kurtosis do not favor a sharp decline in $\rho(r)$, the model requires an even larger dark matter core radius to reproduce the observed kinematics. Allowing r_t to vary as a free parameter, however, permits a small subset of solutions around $m_\psi \sim 10^{-21}$ eV for $r_t/r_c \approx 1$, corresponding to an almost immediate transition from a flat soliton core to an NFW-like profile (Figure 3 lower panel).

The bimodality in m_ψ is not unique to this work and has been reported by K. Hayashi & I. Obata (2020) and I. S. Goldstein et al. (2022). These results likely share a common physical origin as discussed in the previous paragraph. The bimodality further highlights the importance of incorporating an NFW envelope in kinematic analyses of FDM halos. If the dark halo is instead assumed to consist solely of the soliton component, the allowed range of m_ψ becomes restricted to the small- m_ψ solutions because other ranges will place many kinematic samples in the fast declining $\rho(r)$ region beyond r_c . This behavior is apparent in earlier studies such as S.-R. Chen et al. (2017), K. Hayashi & I. Obata (2020), and I. de Martino (2023).

Figure 3 shows the MCMC samples for Draco as a representative example; the other galaxies show broadly

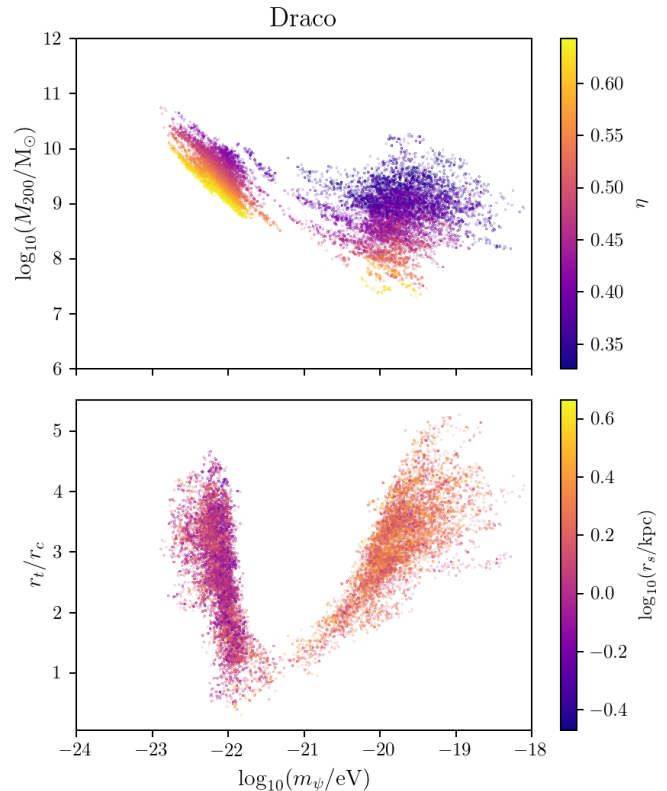


Figure 3. Upper panel: MCMC samples of the estimated $\log_{10}(M_{200})$ versus $\log_{10}(m_\psi/\text{eV})$ for Draco as representative. The colors are coded based on the slope of the CHR η . Lower panel: similar to the upper panel but for r_t/r_c versus $\log_{10}(m_\psi/\text{eV})$ with the colors coded by $\log_{10}(r_s/\text{kpc})$.

similar patterns. The upper panel shows the distribution of samples in the $\log_{10}(M_{200})$ versus $\log_{10}(m_\psi/\text{eV})$ plane, with colors indicating the core–halo mass relation slope, η . A degeneracy between m_ψ and M_{200} —identified by I. S. Goldstein et al. (2022) as the primary driver of the bimodality—is apparent as diagonal patches extending from the upper left to the lower right. This degeneracy is expected and intrinsic to the core–halo mass relation. However, it weakens toward larger m_ψ , since in this regime the soliton core mass M_c contributes less to the total halo mass.

The color coding in the upper panel of Figure 3 further illustrates that, in the absence of diversity in the core–halo mass relation, these diagonal structures would appear as a single, relatively narrow strip (see, for example, the posterior distribution in S.-R. Chen et al. (2017)). Solutions with smaller η are suppressed in the small- m_ψ regime but dominate at larger m_ψ , and vice versa. This behavior follows from Equations (11) and (12), which imply that the central density scales approximately as $\rho_c \propto m_\psi^{6\eta}$. Smaller η therefore mitigates the explosive ρ_c in the large- m_ψ window. For

$\log_{10}(m_\psi/\text{eV}) \gtrsim -19$, ρ_c becomes excessively large to be reconciled with the data, which explains why $\log_{10}(m_\psi/\text{eV}) \gtrsim -19$ is largely disfavored even by CHRs with small η . In the small- m_ψ window, however, small η yields core densities that are too low to be consistent with the observed stellar kinematics.

The lower panel of Figure 3 shows the MCMC solutions in the r_t/r_c versus $\log_{10}(m_\psi/\text{eV})$ plane, with colors indicating $\log_{10}(r_s/\text{kpc})$. A significant correlation is present in the large- m_ψ solution where larger m_ψ values correspond to larger r_t . This trend can be understood as follows. At $\log_{10}(m_\psi/\text{eV}) \approx -21$, the DM core radius is ~ 0.1 kpc, and large r_t/r_c are disfavored because an extended region with $\rho(r) \propto r^{-16}$ would encompass many kinematic samples. As m_ψ increases, however, the core radius shrinks as $r_c \propto m_\psi^{-(3\eta+1)/2}$ and the central density grows as $\rho_c \propto m_\psi^{6\eta}$ (with $\eta \approx 0.3 - 0.6$). The resulting high central densities at large m_ψ require a rapidly declining density profile, making larger values of r_t/r_c increasingly favorable, provided that r_t remains smaller than the projected radii of some of the innermost kinematic samples.

5. DISCUSSION

We summarize our results in Figure 4, which also compiles current constraints on the FDM particle mass. Shaded bands indicate excluded regions, with constraints from this work shown in cyan. The excluded region derived in this work is obtained by directly combining the posterior distributions of m_ψ from all eight dSphs, thereby preserving a conservative statistical treatment throughout the analysis. The allowed ranges we obtain are $-22.1 < \log_{10}(m_\psi/\text{eV}) < -21.5$ ($-22.4 < \log_{10}(m_\psi/\text{eV}) < -21.0$) for the small- m_ψ solution and $-20.3 < \log_{10}(m_\psi/\text{eV}) < -19.2$ ($-20.8 < \log_{10}(m_\psi/\text{eV}) < -18.5$) for the large- m_ψ solution at the 68% (95%) credible intervals. Other bounds derived from kinematical analyses of dwarf galaxies (M. Safarzadeh & D. N. Spergel 2020; S. L. Zoutendijk et al. 2021; K. Hayashi et al. 2021; I. S. Goldstein et al. 2022; T. Zimmermann et al. 2025) are shown in brown. The darker and lighter shades indicate exclusion at the 95% and 68% credible intervals, respectively. The lower portion of the figure includes constraints from a variety of astrophysical and cosmological probes, including the cosmic microwave background and large-scale structure (R. Hlozek et al. 2015; R. Hlozek et al. 2018), the Lyman- α forest (V. Iršič et al. 2017; K. K. Rogers & H. V. Peiris 2021), supermassive black hole superradiance (M. J. Stott & D. J. E. Marsh 2018; H. Davoudiasl & P. B. Denton 2019), kinematics of the Milky Way nuclear star cluster (F. Toguz et al. 2022), perturbations

of stellar streams by dark halos (M. Benito et al. 2020; N. Banik et al. 2021), dynamical heating of UFD stars (N. Dalal & A. Kravtsov 2022; S. May et al. 2025), and Milky Way satellite abundances (D. J. E. Marsh & J. C. Niemeyer 2019; E. O. Nadler et al. 2021). In this part, different tones of gray refer to different works.

Compared to previous constraints derived from dSph kinematics, the large- m_ψ solution obtained in this work is broadly consistent, whereas the small- m_ψ solution is in tension with those results. The latter remains largely allowed in this work due to the inclusion of diversity in the CHR, as illustrated in Figure 3. However, tension persists with constraints based on kinematic studies of UFDs, which are generally more restrictive (K. Hayashi et al. 2021; S. L. Zoutendijk et al. 2021). These tighter bounds arise primarily because dark matter cores with sizes of order hundreds of parsecs are disfavored in halos hosting UFDs.

The tension between constraints from dSphs and UFDs has been discussed previously. For example, M. Safarzadeh & D. N. Spergel (2020) combined arguments based on the CHR and dynamical friction, concluding that no single range of m_ψ can simultaneously fit dSph kinematics while avoid producing implausibly massive UFD host halos ($M \sim 10^{11} - 10^{12} M_\odot$). It is important to emphasize that M. Safarzadeh & D. N. Spergel (2020), S. L. Zoutendijk et al. (2021), and K. Hayashi et al. (2021) all adopt a one-to-one CHR from H.-Y. Schive et al. (2014b). Our results suggest that allowing the recognized diversity in the CHR shifts the lower bounds toward smaller m_ψ because a larger η than that proposed by H.-Y. Schive et al. (2014b) permits lower halo masses without requiring large DM cores. Whether or not the shift can alleviate the tension between dSph and UFD constraints remains to be investigated in future work.

Despite an agreement with constraints from CMB, LSS, and supermassive black hole superradiance, we also note a few interesting conflicts. The first one is tension between the small- m_ψ solution with constraints derived from the abundance of Milky Way satellite galaxies (D. J. E. Marsh & J. C. Niemeyer 2019; E. O. Nadler et al. 2021). In particular, values of m_ψ that generate DM matter cores large enough to explain dSph kinematics also suppress the formation of lower mass halos, reducing the predicted number of satellites below the observed level. Therefore, for less massive systems such as UFDs, small- m_ψ solutions may place FDM in a situation analogous to the well-known “catch-22” faced by simple warm dark matter models (A. V. Macciò et al. 2012), where particle masses low enough to form a sub-

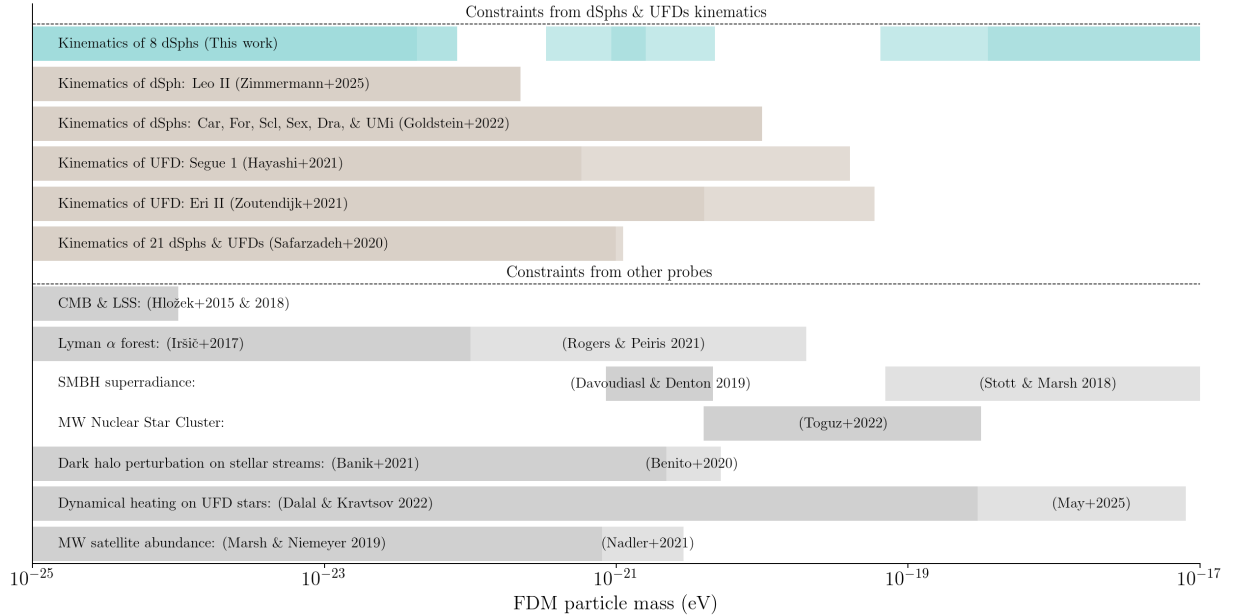


Figure 4. Constraints on the fuzzy dark matter particle mass. The shaded bands indicate excluded ranges of m_ψ . The upper section, in cyan and brown, shows constraints derived from this work and from other kinematic analyses of dwarf galaxies, respectively. Darker and lighter shades show exclusion at 95% and 68% credible intervals, respectively. The lower part, in gray, summarizes constraints obtained from a variety of independent astrophysical and cosmological probes as indicated. Different tones of gray in the same row correspond to different works.

stantial DM core would prevent the formation of the host galaxy itself.

Another interesting tension arises from the large- m_ψ solutions, which are entirely ruled out by the constraints from F. Toguz et al. (2022), who analyzed stellar kinematics in the nuclear star cluster surrounding the Milky Way’s central supermassive black hole. In their excluded m_ψ range, the soliton core is expected to leave a detectable imprint on stellar motions, which has not been observed. For smaller m_ψ , the soliton core density is too low to affect stellar dynamics, while for larger m_ψ , the soliton core mass becomes negligible compared to that of the supermassive black hole. We note, however, that the analysis of F. Toguz et al. (2022) assumes isotropic stellar orbits, $\beta = 0$. A more general dynamical model allowing for anisotropic velocity distributions may yield less restrictive constraints and is required for a more definitive comparison.

The strongest constraints are reported by N. Dalal & A. Kravtsov (2022) and subsequently updated by S. May et al. (2025), both of which examine the spatial distribution of stars in UFDs. These studies analyze the dynamical heating induced by stochastic FDM granules—interference patterns in the dark matter density field that can transfer energy to stars and progressively inflate their orbits. Based on this mechanism, N. Dalal & A. Kravtsov (2022) exclude $m_\psi < 3 \times 10^{-19}$ eV, while S. May et al. (2025), who include the previously ne-

glected nonlinear phenomenon in the simulations, derive a more stringent bound of $m_\psi < 8 \times 10^{-18}$ eV. However, the efficiency of granule-induced heating is not yet fully settled and continues to be explored, with uncertainties in both the theoretical modeling and its implementation in simulations (see e.g., A. Eberhardt et al. (2025) who studied the effect of stellar gravity, tidally stripped halos, and relative size of soliton to stellar distribution on this heating). Moreover, these constraints are inferred from long-term dynamical evolution rather than from instantaneous kinematical measurements, and may therefore be more sensitive to unmodeled processes in the evolutionary history of UFDs (T. Zimmermann et al. 2025).

On the whole, the bounds derived in this work pose a challenge for FDM not only because the small- m_ψ window is in tension with Milky Way satellite abundance constraints, but also because the upper limit of the large- m_ψ window excludes nearly the entire m_ψ parameter space allowed by Lyman- α forest bounds. However, we do not incorporate baryonic effects in this analysis, such as supernova feedback, which has been shown to increase the size of dark matter cores and reduce their central densities (V. H. Robles et al. 2024). If baryonic feedback plays an important role in dSphs, our analysis would underestimate the original central density, implying that the inferred upper limit should shift toward larger m_ψ . Moreover, if future simulations reveal a broader diver-

sity of CHRs, particularly for $\eta \lesssim 1/3$, the upper bound could also shift toward larger m_ψ .

We emphasize that our analysis relies on the assumptions of dynamical equilibrium and spherical symmetry. Although FDM halos are generally found to be more spherical than their CDM counterparts (H.-Y. Schive et al. 2014a), adopting a non-spherical framework would provide a more general and realistic description of the dynamics. Furthermore, simulations indicate that the soliton core undergoes stochastic motion (J. Veltmaat et al. 2018; H.-Y. Schive et al. 2020; D. Dutta Chowdhury et al. 2021), which may influence stellar kinematics but is not accounted for in this analysis.

6. CONCLUSIONS

In this work, we investigate the impact of CHR diversity on the estimation of the FDM particle mass from stellar kinematics in dSph galaxies. The model incorporate not only LOS velocity dispersion but also higher order moments in the form of LOS kurtosis to suppress parameter degeneracy with the velocity anisotropy that was detected in the previous works. We model the dark halo as a soliton core embedded in an NFW halo, with a transition radius set as a free parameter. This model is fit to the observed data of stellar projected position and LOS velocity from eight Milky Way’s dSphs: Carina, Draco, Fornax, Leo I, Leo II, Sculptor, Sextans, and Ursa Minor. We apply the MCMC method to infer the posterior distribution of m_ψ using unbinned analysis.

Our results show that, even after accounting for CHR, the stellar kinematics of dSphs *disfavor*, all within 68% credible intervals:

- (i) $\log_{10}(m_\psi/\text{eV}) < -22.1$, which produces overly extended dark matter cores;
- (ii) $\log_{10}(m_\psi/\text{eV}) > -19.2$, which yields excessively high central densities; and
- (iii) $-21.5 < \log_{10}(m_\psi/\text{eV}) < -20.3$, for which the observed kinematics are inconsistent with residing in the rapidly declining density profile beyond the soliton core predicted for this mass range.

The results of this work pose a challenge to FDM as the small- m_ψ window is in tension with the constraints derived from the Milky Way satellite abundances, and the inferred upper limit almost entirely excludes the parameter space permitted by constraints from Lyman- α forest. This tension may be alleviated if baryonic feedback substantially modifies the internal structure of dSphs, if these systems are undergoing ongoing tidal disruption, and/or if future simulations reveal a broader diversity in the CHR.

ACKNOWLEDGMENTS

We thank Yutaka Hirai for generously providing access to the computational resources used in this work. We are also grateful to Shunichi Horigome, Victor Robles, Hsi-Yu Schive & group members, Tzihong Chiueh, and Andrew Cooper for fruitful discussions. This work was supported by JSPS KAKENHI grant Nos. JP24K00669 and JP25H00394.

AUTHOR CONTRIBUTIONS

All authors contributed equally to this work.

APPENDIX

A. POSTERIOR DISTRIBUTIONS AND RECOVERY OF KINEMATICS

We present the full posterior distributions of all model parameters for each analyzed galaxy in Figures 5 and 6. For reference, we also include the inferred core radius r_c , although it is not treated as a free parameter in the model.

A comparison between the model predictions and the observed kinematic data is shown in Figure 7. The left and right panels display the recovered LOS velocity dispersion and LOS kurtosis profiles for the Draco dSph, respectively. The darker and lighter shaded bands represent the 68% and 95% credible intervals, with green and orange corresponding to the small- and large- m_ψ solutions. The black data points with error bars denote the observed measurements. Although the likelihood analysis is performed using individual stellar measurements without binning, the data are binned in this figure for visualization purposes. The purple curves illustrate model kinematic profiles computed for a fixed value of $\log_{10}(m_\psi/\text{eV}) = -21.4$, while varying the transition radius as $r_t/r_c = [1, 2, 3, 4]$, ordered from the thickest to the thinnest line. These curves illustrate why this range of m_ψ is disfavored by the model.

REFERENCES

- Arroyo-Polonio, J. M., Battaglia, G., Thomas, G. F., et al. 2023, *A&A*, 677, A95, doi: [10.1051/0004-6361/202346843](https://doi.org/10.1051/0004-6361/202346843)
- Bañares-Hernández, A., Read, J. I., & Júlio, M. P. 2025, arXiv e-prints, arXiv:2509.24103, doi: [10.48550/arXiv.2509.24103](https://doi.org/10.48550/arXiv.2509.24103)

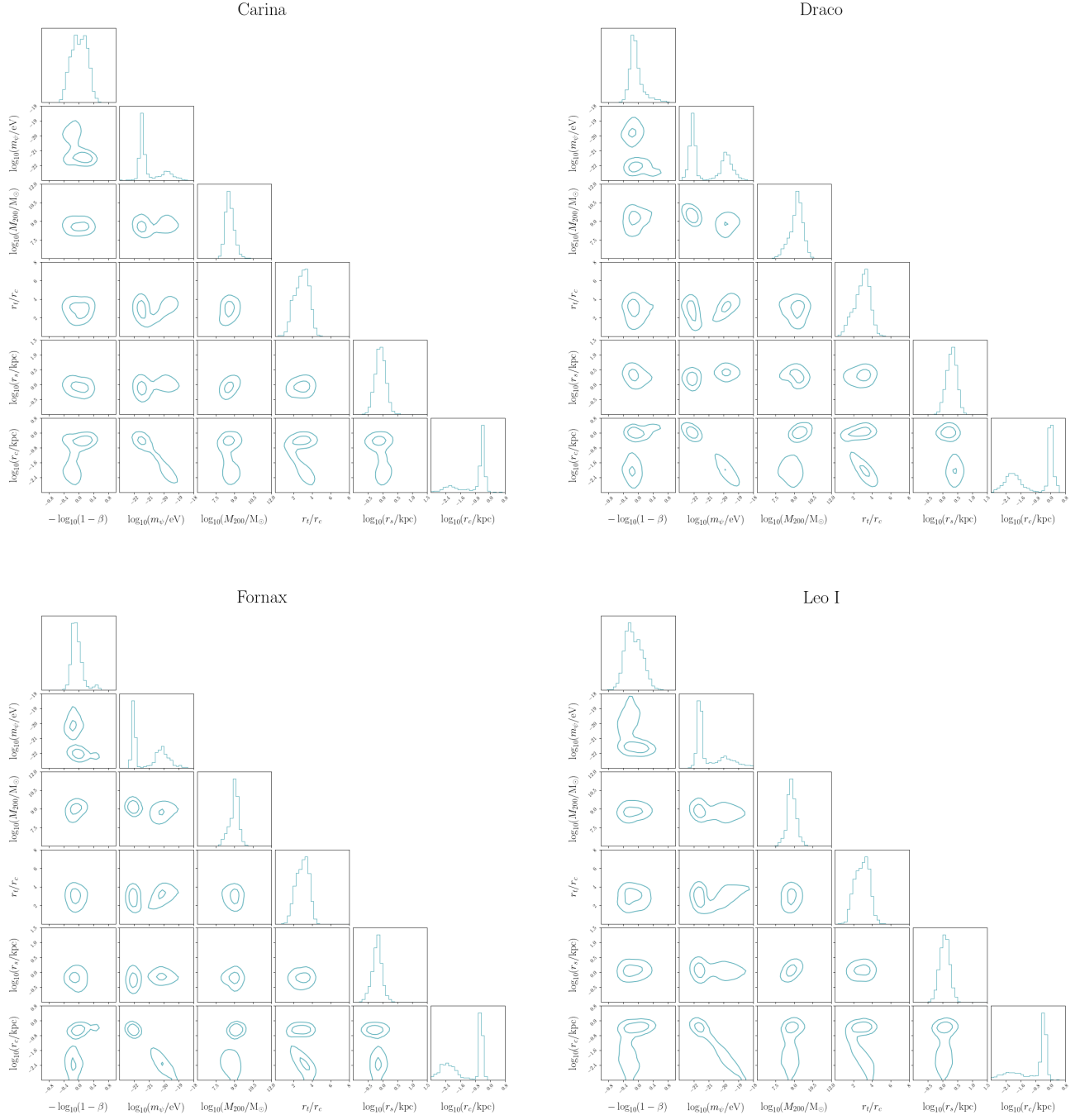


Figure 5. The posterior distributions of the model parameters for Carina, Draco, Fornax, and Leo I. Although r_c is not treated as a free parameter in the model, it is included here for reference.

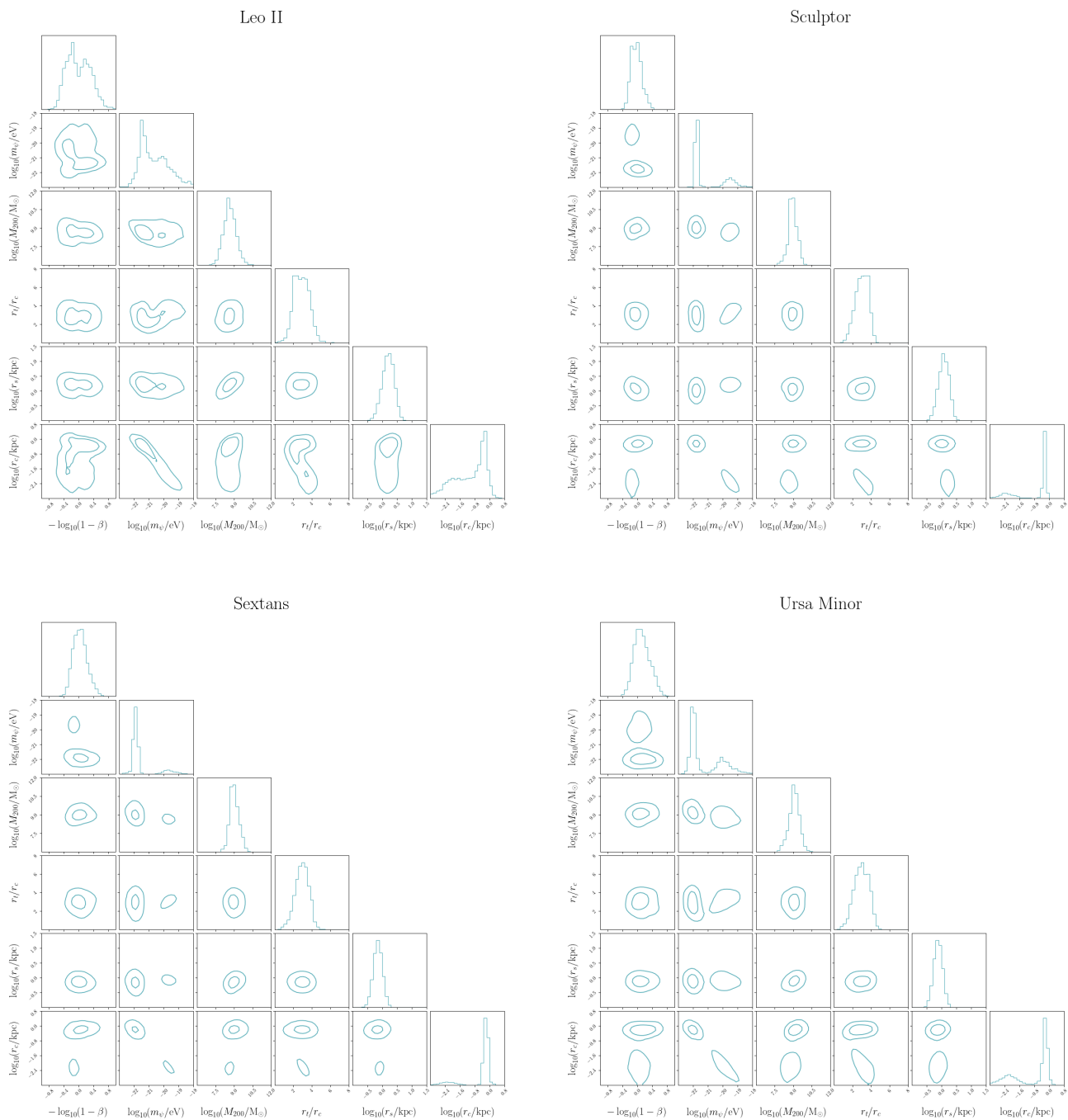


Figure 6. The same as Figure 5, but for Leo II, Sculptor, Sextans, and Ursa Minor.

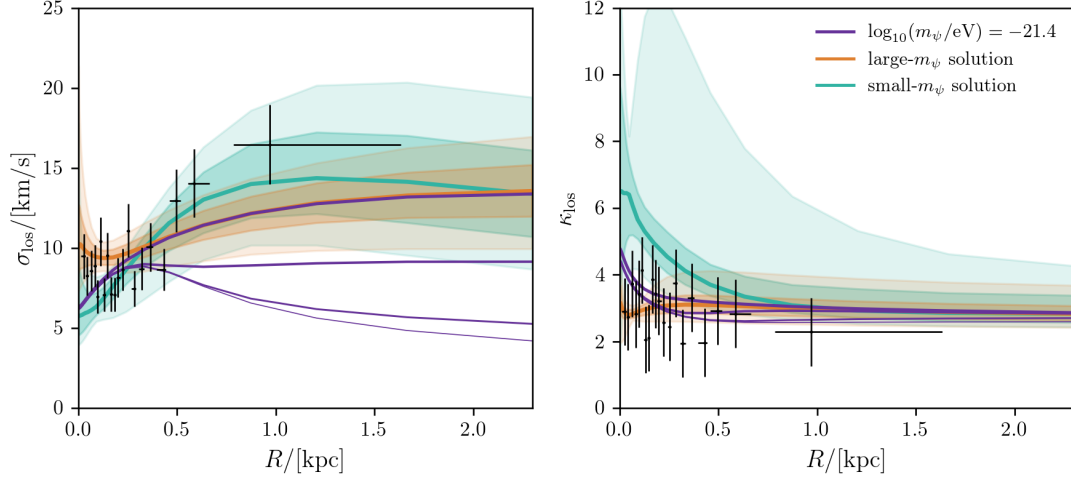


Figure 7. The left and right panels show the recovered LOS velocity dispersion and LOS kurtosis profiles of the Draco dSph, respectively. The darker and lighter shaded bands indicate the 68% and 95% credible intervals, with green and orange corresponding to the small- and large- m_ψ solutions. Purple curves show the predicted σ_{los} and κ_{los} profiles for $\log_{10}(m_\psi/\text{eV}) = -21.4$. The different line thicknesses correspond to $r_t/r_c = [1, 2, 3, 4]$, ordered from the thickest to the thinnest. Black points with error bars denote the observed data, with uncertainties corresponding to the 68% credible intervals.

- Banik, N., Bovy, J., Bertone, G., Erkal, D., & de Boer, T. J. L. 2021, *JCAP*, 2021, 043, doi: [10.1088/1475-7516/2021/10/043](https://doi.org/10.1088/1475-7516/2021/10/043)
- Battaglia, G., Helmi, A., & Breddels, M. 2013, *NewAR*, 57, 52, doi: [10.1016/j.newar.2013.05.003](https://doi.org/10.1016/j.newar.2013.05.003)
- Battaglia, G., & Nipoti, C. 2022, *Nature Astronomy*, 6, 659, doi: [10.1038/s41550-022-01638-7](https://doi.org/10.1038/s41550-022-01638-7)
- Bellazzini, M., Gennari, N., & Ferraro, F. R. 2005, *MNRAS*, 360, 185, doi: [10.1111/j.1365-2966.2005.09027.x](https://doi.org/10.1111/j.1365-2966.2005.09027.x)
- Bellazzini, M., Gennari, N., Ferraro, F. R., & Sollima, A. 2004, *Monthly Notices of the Royal Astronomical Society*, 354, 708, doi: [10.1111/j.1365-2966.2004.08226.x](https://doi.org/10.1111/j.1365-2966.2004.08226.x)
- Benito, M., Criado, J. C., Hütsi, G., Raidal, M., & Veermäe, H. 2020, *PhRvD*, 101, 103023, doi: [10.1103/PhysRevD.101.103023](https://doi.org/10.1103/PhysRevD.101.103023)
- Binney, J., & Merrifield, M. 1998, *Galactic Astronomy* (Princeton University Press)
- Binney, J., & Tremaine, S. 2008, *Galactic Dynamics: Second Edition* (Princeton University Press)
- Bonanos, A. Z., Stanek, K. Z., Szentgyorgyi, A. H., Sasselov, D. D., & Bakos, G. Á. 2004, *The Astronomical Journal*, 127, 861, doi: [10.1086/381073](https://doi.org/10.1086/381073)
- Bullock, J. S., & Boylan-Kolchin, M. 2017, *Annual Review of Astronomy and Astrophysics*, 55, 343, doi: [10.1146/annurev-astro-091916-055313](https://doi.org/10.1146/annurev-astro-091916-055313)
- Carrera, R., Aparicio, A., Martínez-Delgado, D., & Alonso-García, J. 2002, *The Astronomical Journal*, 123, 3199, doi: [10.1086/340702](https://doi.org/10.1086/340702)
- Chan, H. Y. J., Ferreira, E. G. M., May, S., Hayashi, K., & Chiba, M. 2022, *MNRAS*, 511, 943, doi: [10.1093/mnras/stac063](https://doi.org/10.1093/mnras/stac063)
- Chen, S.-R., Schive, H.-Y., & Chiueh, T. 2017, *MNRAS*, 468, 1338, doi: [10.1093/mnras/stx449](https://doi.org/10.1093/mnras/stx449)
- Dalal, N., & Kravtsov, A. 2022, *Physical Review D*, 106, 063517, doi: [10.1103/PhysRevD.106.063517](https://doi.org/10.1103/PhysRevD.106.063517)
- Davoudiasl, H., & Denton, P. B. 2019, *PhRvL*, 123, 021102, doi: [10.1103/PhysRevLett.123.021102](https://doi.org/10.1103/PhysRevLett.123.021102)
- de Martino, I. 2023, *PhRvD*, 108, 123044, doi: [10.1103/PhysRevD.108.123044](https://doi.org/10.1103/PhysRevD.108.123044)
- Dutta Chowdhury, D., van den Bosch, F. C., Robles, V. H., et al. 2021, *ApJ*, 916, 27, doi: [10.3847/1538-4357/ac043f](https://doi.org/10.3847/1538-4357/ac043f)
- Eberhardt, A., & Ferreira, E. G. M. 2025, arXiv e-prints, arXiv:2507.00705, doi: [10.48550/arXiv.2507.00705](https://doi.org/10.48550/arXiv.2507.00705)
- Eberhardt, A., Gosenca, M., & Hui, L. 2025, arXiv e-prints, arXiv:2510.17079, doi: [10.48550/arXiv.2510.17079](https://doi.org/10.48550/arXiv.2510.17079)
- Fabrizio, M., Bono, G., Nonino, M., et al. 2016, *The Astrophysical Journal*, 830, 126, doi: [10.3847/0004-637X/830/2/126](https://doi.org/10.3847/0004-637X/830/2/126)
- Ferreira, E. G. M. 2021, *Astronomy & Astrophysics Review*, 29, 7, doi: [10.1007/s00159-021-00135-6](https://doi.org/10.1007/s00159-021-00135-6)
- Genina, A., Read, J. I., Frenk, C. S., et al. 2020, *MNRAS*, 498, 144, doi: [10.1093/mnras/staa2352](https://doi.org/10.1093/mnras/staa2352)
- Goldstein, I. S., Koushiappas, S. M., & Walker, M. G. 2022, *PhRvD*, 106, 063010, doi: [10.1103/PhysRevD.106.063010](https://doi.org/10.1103/PhysRevD.106.063010)
- González-Morales, A. X., Marsh, D. J. E., Peñarrubia, J., & Ureña-López, L. A. 2017, *MNRAS*, 472, 1346, doi: [10.1093/mnras/stx1941](https://doi.org/10.1093/mnras/stx1941)
- Hastings, W. K. 1970, *Biometrika*, 57, 97, doi: [10.1093/biomet/57.1.97](https://doi.org/10.1093/biomet/57.1.97)
- Hayashi, K., Ferreira, E. G. M., & Chan, H. Y. J. 2021, *ApJL*, 912, L3, doi: [10.3847/2041-8213/abf501](https://doi.org/10.3847/2041-8213/abf501)

- Hayashi, K., & Obata, I. 2020, *MNRAS*, 491, 615, doi: [10.1093/mnras/stz2950](https://doi.org/10.1093/mnras/stz2950)
- Hložek, R., Marsh, D. J. E., & Grin, D. 2018, *Monthly Notices of the Royal Astronomical Society*, 476, 3063, doi: [10.1093/mnras/sty271](https://doi.org/10.1093/mnras/sty271)
- Hložek, R., Grin, D., Marsh, D. J. E., & Ferreira, P. G. 2015, *Physical Review D*, 91, 103512, doi: [10.1103/PhysRevD.91.103512](https://doi.org/10.1103/PhysRevD.91.103512)
- Hu, W., Barkana, R., & Gruzinov, A. 2000, *Physical Review Letters*, 85, 1158, doi: [10.1103/PhysRevLett.85.1158](https://doi.org/10.1103/PhysRevLett.85.1158)
- Hui, L. 2021, *ARA&A*, 59, 247, doi: [10.1146/annurev-astro-120920-010024](https://doi.org/10.1146/annurev-astro-120920-010024)
- Hui, L., Ostriker, J. P., Tremaine, S., & Witten, E. 2017, *PhRvD*, 95, 043541, doi: [10.1103/PhysRevD.95.043541](https://doi.org/10.1103/PhysRevD.95.043541)
- Iršič, V., Viel, M., Haehnelt, M. G., Bolton, J. S., & Becker, G. D. 2017, *PhRvL*, 119, 031302, doi: [10.1103/PhysRevLett.119.031302](https://doi.org/10.1103/PhysRevLett.119.031302)
- Ishiyama, T., Prada, F., Klypin, A. A., et al. 2021, *MNRAS*, 506, 4210, doi: [10.1093/mnras/stab1755](https://doi.org/10.1093/mnras/stab1755)
- Kawai, H., Kamada, A., Kamada, K., & Yoshida, N. 2024, *PhRvD*, 110, 023519, doi: [10.1103/PhysRevD.110.023519](https://doi.org/10.1103/PhysRevD.110.023519)
- Kirby, E. N., Boylan-Kolchin, M., Cohen, J. G., et al. 2013, *ApJ*, 770, 16, doi: [10.1088/0004-637X/770/1/16](https://doi.org/10.1088/0004-637X/770/1/16)
- Kirby, E. N., Cohen, J. G., Simon, J. D., et al. 2017, *ApJ*, 838, 83, doi: [10.3847/1538-4357/aa6570](https://doi.org/10.3847/1538-4357/aa6570)
- Koch, A., Kley, J. T., Wilkinson, M. I., et al. 2007, *The Astronomical Journal*, 134, 566, doi: [10.1086/519380](https://doi.org/10.1086/519380)
- Laroche, A., Gilman, D., Li, X., Bovy, J., & Du, X. 2022, *MNRAS*, 517, 1867, doi: [10.1093/mnras/stac2677](https://doi.org/10.1093/mnras/stac2677)
- Lee, M. G., Yuk, I.-S., Park, H. S., Harris, J., & Zaritsky, D. 2009, *The Astrophysical Journal*, 703, 692, doi: [10.1088/0004-637X/703/1/692](https://doi.org/10.1088/0004-637X/703/1/692)
- Liao, P.-Y., Su, G.-M., Schive, H.-Y., et al. 2025, *PhRvL*, 135, 061002, doi: [10.1103/9dqj-q6mt](https://doi.org/10.1103/9dqj-q6mt)
- Łokas, E. L. 2002, *MNRAS*, 333, 697, doi: [10.1046/j.1365-8711.2002.05457.x](https://doi.org/10.1046/j.1365-8711.2002.05457.x)
- Macciò, A. V., Paduroiu, S., Anderhalden, D., Schneider, A., & Moore, B. 2012, *MNRAS*, 424, 1105, doi: [10.1111/j.1365-2966.2012.21284.x](https://doi.org/10.1111/j.1365-2966.2012.21284.x)
- María Arroyo-Polonio, J., Battaglia, G., & Thomas, G. F. 2026, arXiv e-prints, arXiv:2603.03129, doi: [10.48550/arXiv.2603.03129](https://doi.org/10.48550/arXiv.2603.03129)
- Marsh, D. J. E., & Niemeyer, J. C. 2019, *PhRvL*, 123, 051103, doi: [10.1103/PhysRevLett.123.051103](https://doi.org/10.1103/PhysRevLett.123.051103)
- Mateo, M., Olszewski, E. W., & Walker, M. G. 2008, *The Astrophysical Journal*, 675, 201, doi: [10.1086/522326](https://doi.org/10.1086/522326)
- May, S., Dalal, N., & Kravtsov, A. 2025, arXiv e-prints, arXiv:2509.02781, doi: [10.48550/arXiv.2509.02781](https://doi.org/10.48550/arXiv.2509.02781)
- May, S., & Springel, V. 2021, *MNRAS*, 506, 2603, doi: [10.1093/mnras/stab1764](https://doi.org/10.1093/mnras/stab1764)
- McConnachie, A. W. 2012, *The Astronomical Journal*, 144, 4, doi: [10.1088/0004-6256/144/1/4](https://doi.org/10.1088/0004-6256/144/1/4)
- McConnachie, A. W., & Côté, P. 2010, *ApJL*, 722, L209, doi: [10.1088/2041-8205/722/2/L209](https://doi.org/10.1088/2041-8205/722/2/L209)
- Merrifield, M. R., & Kent, S. M. 1990, in *Bulletin of the American Astronomical Society*, Vol. 22, 744
- Metropolis, N., Rosenbluth, A. W., Rosenbluth, M. N., Teller, A. H., & Teller, E. 1953, *JChPh*, 21, 1087, doi: [10.1063/1.1699114](https://doi.org/10.1063/1.1699114)
- Mina, M., Mota, D. F., & Winther, H. A. 2022, *A&A*, 662, A29, doi: [10.1051/0004-6361/202038876](https://doi.org/10.1051/0004-6361/202038876)
- Minor, Q. E. 2013, *ApJ*, 779, 116, doi: [10.1088/0004-637X/779/2/116](https://doi.org/10.1088/0004-637X/779/2/116)
- Mocz, P., Vogelsberger, M., Robles, V. H., et al. 2017, *MNRAS*, 471, 4559, doi: [10.1093/mnras/stx1887](https://doi.org/10.1093/mnras/stx1887)
- Moliné, Á., Sánchez-Conde, M. A., Palomares-Ruiz, S., & Prada, F. 2017, *MNRAS*, 466, 4974, doi: [10.1093/mnras/stx026](https://doi.org/10.1093/mnras/stx026)
- Muñoz, R. R., Côté, P., Santana, F. A., et al. 2018, *The Astrophysical Journal*, 860, 66, doi: [10.3847/1538-4357/aac16b](https://doi.org/10.3847/1538-4357/aac16b)
- Nadler, E. O., Drlica-Wagner, A., Bechtol, K., et al. 2021, *PhRvL*, 126, 091101, doi: [10.1103/PhysRevLett.126.091101](https://doi.org/10.1103/PhysRevLett.126.091101)
- Navarro, J. F., Frenk, C. S., & White, S. D. M. 1997, *The Astrophysical Journal*, 490, 493, doi: [10.1086/304888](https://doi.org/10.1086/304888)
- Nori, M., & Baldi, M. 2021, *MNRAS*, 501, 1539, doi: [10.1093/mnras/staa3772](https://doi.org/10.1093/mnras/staa3772)
- Pianta, C., Capuzzo-Dolcetta, R., & Carraro, G. 2022, *ApJ*, 939, 3, doi: [10.3847/1538-4357/ac9303](https://doi.org/10.3847/1538-4357/ac9303)
- Pietrzyński, G., Górski, M., Gieren, W., et al. 2009, *AJ*, 138, 459, doi: [10.1088/0004-6256/138/2/459](https://doi.org/10.1088/0004-6256/138/2/459)
- Pietrzyński, G., Gieren, W., Szewczyk, O., et al. 2008, *The Astronomical Journal*, 135, 1993, doi: [10.1088/0004-6256/135/6/1993](https://doi.org/10.1088/0004-6256/135/6/1993)
- Plummer, H. C. 1911, *MNRAS*, 71, 460, doi: [10.1093/mnras/71.5.460](https://doi.org/10.1093/mnras/71.5.460)
- Prada, F., Klypin, A. A., Cuesta, A. J., Betancort-Rijo, J. E., & Primack, J. 2012, *MNRAS*, 423, 3018, doi: [10.1111/j.1365-2966.2012.21007.x](https://doi.org/10.1111/j.1365-2966.2012.21007.x)
- Read, J. I., Mamon, G. A., Vasiliev, E., et al. 2021, *MNRAS*, 501, 978, doi: [10.1093/mnras/staa3663](https://doi.org/10.1093/mnras/staa3663)
- Robles, V. H., & Matos, T. 2012, *MNRAS*, 422, 282, doi: [10.1111/j.1365-2966.2012.20603.x](https://doi.org/10.1111/j.1365-2966.2012.20603.x)
- Robles, V. H., Zagorac, J. L., & Padmanabhan, N. 2024, *MNRAS*, 532, 1980, doi: [10.1093/mnras/stae1544](https://doi.org/10.1093/mnras/stae1544)
- Rogers, K. K., & Peiris, H. V. 2021, *Physical Review Letters*, 126, 071302, doi: [10.1103/PhysRevLett.126.071302](https://doi.org/10.1103/PhysRevLett.126.071302)

- Safarzadeh, M., & Spergel, D. N. 2020, *ApJ*, 893, 21, doi: [10.3847/1538-4357/ab7db2](https://doi.org/10.3847/1538-4357/ab7db2)
- Sanders, J. L., & Evans, N. W. 2020, *MNRAS*, 499, 5806, doi: [10.1093/mnras/staa2860](https://doi.org/10.1093/mnras/staa2860)
- Schive, H.-Y., Chiueh, T., & Broadhurst, T. 2014a, *Nature Physics*, 10, 496, doi: [10.1038/nphys2996](https://doi.org/10.1038/nphys2996)
- Schive, H.-Y., Chiueh, T., & Broadhurst, T. 2020, *PhRvL*, 124, 201301, doi: [10.1103/PhysRevLett.124.201301](https://doi.org/10.1103/PhysRevLett.124.201301)
- Schive, H.-Y., Liao, M.-H., Woo, T.-P., et al. 2014b, *PhRvL*, 113, 261302, doi: [10.1103/PhysRevLett.113.261302](https://doi.org/10.1103/PhysRevLett.113.261302)
- Schwabe, B., Niemeyer, J. C., & Engels, J. F. 2016, *Physical Review D*, 94, 043513, doi: [10.1103/PhysRevD.94.043513](https://doi.org/10.1103/PhysRevD.94.043513)
- Spencer, M. E., Mateo, M., Olszewski, E. W., et al. 2018, *The Astronomical Journal*, 156, 257, doi: [10.3847/1538-3881/aae3e4](https://doi.org/10.3847/1538-3881/aae3e4)
- Spencer, M. E., Mateo, M., Walker, M. G., & Olszewski, E. W. 2017, *ApJ*, 836, 202, doi: [10.3847/1538-4357/836/2/202](https://doi.org/10.3847/1538-4357/836/2/202)
- Stott, M. J., & Marsh, D. J. E. 2018, *PhRvD*, 98, 083006, doi: [10.1103/PhysRevD.98.083006](https://doi.org/10.1103/PhysRevD.98.083006)
- Takada, M., Ellis, R. S., Chiba, M., et al. 2014, *Publications of the Astronomical Society of Japan*, 66, R1, doi: [10.1093/pasj/pst019](https://doi.org/10.1093/pasj/pst019)
- Tamura, N., Takato, N., Shimono, A., et al. 2016, in *Society of Photo-Optical Instrumentation Engineers (SPIE) Conference Series*, Vol. 9908, *Ground-based and Airborne Instrumentation for Astronomy VI*, ed. C. J. Evans, L. Simard, & H. Takami, 99081M, doi: [10.1117/12.2232103](https://doi.org/10.1117/12.2232103)
- Toguz, F., Kawata, D., Seabroke, G., & Read, J. I. 2022, *MNRAS*, 511, 1757, doi: [10.1093/mnras/stac057](https://doi.org/10.1093/mnras/stac057)
- Totani, T. 2025, *JCAP*, 2025, 080, doi: [10.1088/1475-7516/2025/11/080](https://doi.org/10.1088/1475-7516/2025/11/080)
- Veltmaat, J., Niemeyer, J. C., & Schwabe, B. 2018, *PhRvD*, 98, 043509, doi: [10.1103/PhysRevD.98.043509](https://doi.org/10.1103/PhysRevD.98.043509)
- Walker, M. G., Mateo, M., & Olszewski, E. W. 2009a, *The Astronomical Journal*, 137, 3100, doi: [10.1088/0004-6256/137/2/3100](https://doi.org/10.1088/0004-6256/137/2/3100)
- Walker, M. G., Mateo, M., Olszewski, E. W., Sen, B., & Woodroffe, M. 2009b, *The Astronomical Journal*, 137, 3109, doi: [10.1088/0004-6256/137/2/3109](https://doi.org/10.1088/0004-6256/137/2/3109)
- Walker, M. G., Olszewski, E. W., & Mateo, M. 2015, *VizieR Online Data Catalog*, *J/MNRAS/448/2717*
- Wang, W., Zhu, L., Jing, Y., et al. 2023, *ApJ*, 956, 91, doi: [10.3847/1538-4357/acf314](https://doi.org/10.3847/1538-4357/acf314)
- Wardana, D., Chiba, M., & Hayashi, K. 2025, *ApJ*, 982, 167, doi: [10.3847/1538-4357/adb8e4](https://doi.org/10.3847/1538-4357/adb8e4)
- Zimmermann, T., Alvey, J., Marsh, D. J. E., Fairbairn, M., & Read, J. I. 2025, *Physical Review Letters*, 134, 151001, doi: [10.1103/PhysRevLett.134.151001](https://doi.org/10.1103/PhysRevLett.134.151001)
- Zoutendijk, S. L., Brinchmann, J., Bouché, N. F., et al. 2021, *A&A*, 651, A80, doi: [10.1051/0004-6361/202040239](https://doi.org/10.1051/0004-6361/202040239)